

# GRASP: Guided Residual Adapters with Sample-wise Partitioning

Felix Nützel<sup>1</sup> Mischa Dombrowski<sup>1</sup> Bernhard Kainz<sup>1,2</sup>

<sup>1</sup>Friedrich-Alexander-Universität Erlangen-Nürnberg <sup>2</sup>Imperial College London

felix.nuetzel@fau.de

## Abstract

Recent advances in text-to-image diffusion models enable high-fidelity generation across diverse prompts. However, these models falter in long-tail settings, such as medical imaging, where rare pathologies comprise a small fraction of data. This results in mode collapse: tail-class outputs lack quality and diversity, undermining the goal of synthetic data augmentation for underrepresented conditions. We pinpoint gradient conflicts between frequent head and rare tail classes as the primary culprit, a factor unaddressed by existing sampling or conditioning methods that mainly steer inference without altering the learned distribution. To resolve this, we propose GRASP: Guided Residual Adapters with Sample-wise Partitioning. GRASP uses external priors to statically partition samples into clusters that minimize intra-group gradient clashes. It then fine-tunes pre-trained models by injecting cluster-specific residual adapters into transformer feedforward layers, bypassing learned gating for stability and efficiency. On the long-tail MIMIC-CXR-LT dataset, GRASP yields superior FID and diversity metrics, especially for rare classes, outperforming baselines like vanilla fine-tuning and Mixture of Experts variants. Downstream classification on NIH-CXR-LT improves considerably for tail labels. Generalization to ImageNet-LT confirms broad applicability. Our method is lightweight, scalable, and readily integrates with diffusion pipelines.

## 1. Introduction

Text-to-image diffusion models have transformed visual generation by enabling controllable and photorealistic synthesis at scale. Yet, their performance degrades markedly in long-tail distributions, where rare classes dominate real-world scenarios, like medical imaging. In such settings, models prioritize frequent head classes, leading to mode collapse in tail classes: generated images for rare pathologies exhibit poor fidelity and severely limited diversity. The result is a systematic collapse of diversity in rare conditions, which limits the potential of synthetic data augmentation

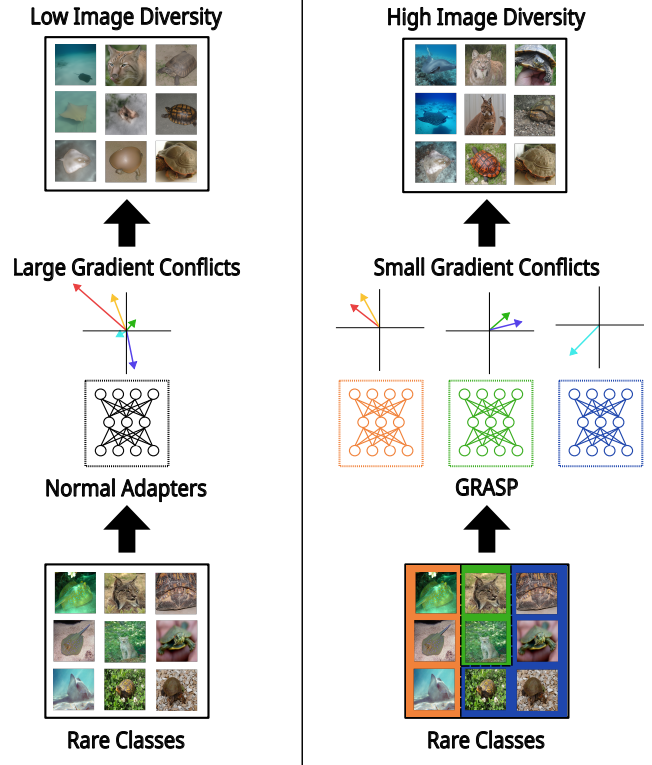


Figure 1. Our proposed method uses parallel GRASP adapters to lessen the impact of gradient conflicts when training a diffusion transformer. This enables the model to generate images of higher quality and diversity, in particular for rare classes.

and undermines downstream robustness. This hampers critical applications, such as augmenting datasets for underrepresented diseases, where diverse, high-quality synthetics are essential for robust training.

Prior efforts to mitigate this focus on post-hoc sampling strategies that guide inference toward underrepresented modes [25, 31, 33, 34]. While effective for exploration, these techniques leave the underlying distribution unchanged, failing to prevent conditional mode collapse during training [1]. Recent diversity enhancements in

diffusion models [3, 23, 38] improve overall coverage but overlook the core issue: gradient conflicts between head and tail classes. Analyses in classification and language tasks reveal that mismatched gradient norms and directions, coupled with noisy tail-class signals, disrupt optimization in imbalanced data [4, 7]. Surprisingly, this fundamental challenge remains unaddressed in generative long-tail settings, where tail-class underrepresentation exacerbates distribution shifts.

We bridge this gap with GRASP: Guided Residual Adapters with Sample-wise Partitioning. As displayed in Figure 1, GRASP imposes a static external prior to partition training samples into semantically coherent clusters (*e.g.*, head, medium, tail and healthy via labels or text embeddings), isolating gradient updates to minimize intra-cluster conflicts. During fine-tuning of a frozen pre-trained backbone, cluster-specific residual adapters (lightweight non-linear skips inserted into feedforward layers) enable targeted refinement without learned routing. This preserves the original generation objective while enhancing stability and efficiency.

Our approach delivers clear and consistent improvements across challenging long-tail benchmarks. On MIMIC-CXR-LT, GRASP reduces overall FID by up to 80% and increases tail-class diversity metrics such as coverage by up to 44% compared to state-of-the-art baselines. When GRASP-generated images are used for downstream classification on NIH-CXR-LT, the F1-score for rare labels improves by up to 6 percentage points. Extensive ablations confirm that both the sample-wise partitioning and the residual adapter design are essential to these gains. Importantly, the benefits extend beyond medical imaging: results on ImageNet-LT demonstrate that GRASP generalizes to broad long-tail generation tasks. In summary, our contributions are:

- We introduce the first method that directly mitigates gradient conflicts in long-tail text-to-image training through prior-guided sample partitioning, addressing mode collapse at its origin.
- We present GRASP, a lightweight and routing-free residual adapter framework that fine-tunes diffusion transformers for balanced, high-fidelity, and diverse synthesis in imbalanced domains.
- We provide comprehensive validation across medical (MIMIC-CXR-LT and NIH-CXR-LT) and general (ImageNet-LT) benchmarks, showing substantial gains in visual quality, diversity, and downstream utility.

## 2. Related Work

**Conditional guidance in diffusion models.** We introduce a sample-wise prior during training, conceptually related to conditional guidance that biases generation toward class or text priors. Class- and text-conditioning are stan-

dard in diffusion models, typically realized via Classifier-Free Guidance (CFG) [2, 11, 30]. Prior methods mainly steer inference through external guidance without modifying the learned distribution [23, 25, 31, 33, 34, 38]. Recent training-time techniques directly address long-tail imbalance: Contrastive Conditional-Unconditional Alignment (CCUA) aligns conditional and unconditional objectives to transfer knowledge from head to tail classes [20], while Generative Active Learning performs failure-aware on-policy augmentation via controllable diffusion [28]. In contrast, GRASP isolates conflicting gradients architecturally rather than aligning them, using a static, prior-guided partition that integrates seamlessly with CFG, as verified in our experiments.

**Mixture-of-Experts.** Expert layers expand model capacity by sparsifying computation through a gating function [32]. For long-tail learning, Cluster-Guided Sparse Experts condition routing on feature centroids [4], Meta-Experts assign head/medium/tail samples via a feature-based module [13], and hypernetwork-generated experts adapt to test-time distributions [39]. Another family replaces dense layers with adapter-based experts using LoRA [14], such as Mixture of LoRA Experts [16], ensembles of low-rank adapters [19], and cluster-conditional variants like MoCLE [9]. Within diffusion transformers, MoE extensions have achieved state-of-the-art scaling: RAPHAEL stacks diffusion paths for large text-to-image models [36], Dense2MoE converts dense FLUX transformers into sparse experts [40], and DiffPruning forms timestep-specific experts [8]. ProMoE [6] further introduces semantic super-class partitions with explicit routing losses. GRASP advances this paradigm: when strong priors exist, learned routing becomes unnecessary. Our static, prior-guided multiplexer replaces the gating network entirely, specializing experts by data partition instead of token or timestep, reducing complexity and stabilizing training while remaining fully compatible with existing conditioning schemes.

**Generative models for long-tail medical imaging.** Recent work targets rare pathology synthesis and class imbalance in medical diffusion. Text-guided latent diffusion improves disease classification in pediatric chest X-rays [29], while feature-space augmentation with sparse latent mixing enhances minority coverage [5]. Lesion-focused objectives in LeFusion enable controllable pathology synthesis under extreme imbalance [37], and causal disentanglement of structure and pathology yields more robust long-tail generation [24]. Unlike these task-specific models that alter diffusion objectives or latent factorization, GRASP introduces a general architectural fine-tuning mechanism that mitigates tail-class collapse at its optimization origin through prior-guided expert isolation, validated on both medical (MIMIC-CXR-LT) and general (ImageNet-LT) domains.

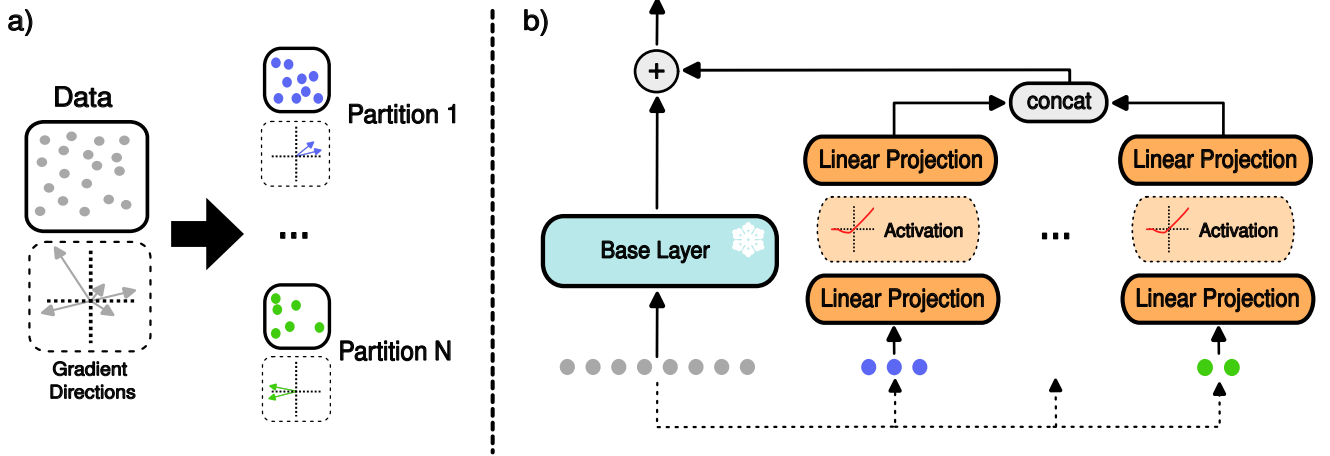


Figure 2. Overview of the GRASP architecture: **a)** We want to minimize gradient conflicts during training partitioning the samples into subsets with aligned gradient directions. **b)** Based on this partitioning, we deterministically route samples to their designated expert, while keeping the base model frozen.

### 3. Method

**Sample-wise Partitioning.** As illustrated in Figure 2a, our objective is to construct a partitioning function  $\pi : \mathcal{X} \rightarrow \{1, \dots, K\}$  that assigns each training sample  $x_i$  to one of  $K$  expert subsets such that the expected pairwise gradient conflict within each subset is minimized:

$$\pi^* = \arg \min_{\pi} \mathbb{E}_{i,j \sim \pi^{-1}(k)} [1 - \cos(\nabla_{\theta} \mathcal{L}(x_i), \nabla_{\theta} \mathcal{L}(x_j))], \quad (1)$$

where  $\mathcal{L}$  denotes the per-sample loss and  $\nabla_{\theta} \mathcal{L}(x_i)$  its gradient with respect to model parameters  $\theta$ . Equation 1 formalizes our central principle: samples whose gradients are directionally aligned should be optimized together, while conflicting ones should be separated across experts.

A direct realization of Eq. 1 would require explicit gradient computation for every sample at each iteration, followed by online clustering in gradient space. Such a strategy, although conceptually optimal, is computationally intractable for high-dimensional diffusion transformers, as gradient vectors evolve rapidly and layer-wise projections or approximations incur prohibitive overhead.

To obtain a tractable surrogate, we approximate gradient similarity via a semantic proxy. Let  $f(x_i)$  represent a semantic feature embedding that captures the high-level structure to be generated (e.g., anatomical or textual content). Assuming that semantically similar samples yield correlated gradients, i.e.  $\cos(\nabla_{\theta} \mathcal{L}(x_i), \nabla_{\theta} \mathcal{L}(x_j)) \propto \cos(f(x_i), f(x_j))$ , we relax Eq. 1 to

$$\pi^* \approx \arg \min_{\pi} \mathbb{E}_{i,j \sim \pi^{-1}(k)} [1 - \cos(f(x_i), f(x_j))]. \quad (2)$$

This approximation transforms the intractable gradient-space optimization into a low-cost clustering problem in semantic space.

In text-to-image diffusion, explicit image features  $f(x_i)$  are unavailable prior to generation. We therefore use dataset priors as external surrogates for  $f(x_i)$ . Specifically, we exploit label semantics as a discrete embedding space  $\ell(x_i)$  and define

$$f(x_i) = \phi(\ell(x_i)), \quad (3)$$

where  $\phi(\cdot)$  maps labels to semantic vector representations. This yields a stable, prior-guided static partition  $\pi_{\ell}$  that requires no online recomputation and reflects the intrinsic long-tail structure of the dataset.

A straightforward partitioning approach is to distribute samples into  $K = 3$  balanced semantic clusters corresponding to head, medium, and tail frequency regimes, following established heuristics [13, 39]. Medical imaging further offers a domain-specific inductive bias: a natural dichotomy between normal and pathological samples. We therefore introduce an additional cluster  $\pi_{\text{healthy}}$  to MIMIC-CXR-LT [12], containing all healthy cases, yielding a four-expert configuration that explicitly disentangles normative and abnormal anatomical distributions. This domain-aware extension is a key novelty of our approach, as it formalizes a biologically meaningful proxy for gradient alignment while remaining computationally negligible.

While label-based partitioning provides a coarse yet interpretable structure, it ignores intra-label semantic distances. To refine cluster cohesion, we extend our approach with text-embedding features:  $f(x_i) = \psi(t_i)$ , where  $t_i$  is the paired textual prompt and  $\psi(\cdot)$  denotes the frozen text encoder of the diffusion backbone. We then compute  $\pi_{\text{text}}$  by minimizing Eq. 2 using bisecting  $K$ -means on  $\{f(x_i)\}$ , preserving the four-expert configuration ( $K = 4$ ). Figure 3 visualizes the resulting cluster compositions for both label- and text-based strategies.

For ImageNet-LT, where 1,000 unique labels render  $\pi_\ell$  infeasible, we rely solely on text-embedding clustering, demonstrating that our approach generalizes naturally beyond medical domains.

**Guided Residual Adapters.** Given the static partitioning function  $\pi : \mathcal{X} \rightarrow \{1, \dots, K\}$  defined above, we now condition the model architecture on these partitions via guided residual adapters. Unlike conventional MoE approaches that employ a learned gating function  $g(x_i)$  to assign tokens or samples to experts [4, 32], our design eliminates gating entirely. Instead, each sample  $x_i$  is deterministically routed to a fixed expert  $E_{\pi(x_i)}$  according to its partition label. This removes the stochasticity and instability of soft routing.

The hidden representation at transformer block  $l$  is denoted by  $h_l \in \mathbb{R}^d$ , and the corresponding base FeedForward transformation is  $F_l(h_l)$ . We augment this block with a residual adapter  $A_{k,l}$  that is specific to expert  $k = \pi(x_i)$ . The layer output for a given sample  $x_i$  thus becomes

$$h_{l+1} = F_l(h_l) + A_{\pi(x_i),l}(h_l), \quad (4)$$

where  $A_{\pi(x_i),l}$  represents the guided residual adapter associated with the expert selected by the static prior. This residual formulation allows the model to specialize adapter weights per expert while preserving a shared backbone for generalization. Each adapter is parameterized as a two-layer transformation:

$$A_{k,l}(h) = W_{k,l}^{(2)} \sigma(W_{k,l}^{(1)} h), \quad (5)$$

where  $\sigma(\cdot)$  denotes a non-linearity and  $(W_{k,l}^{(1)}, W_{k,l}^{(2)})$  are the down- and up-projection matrices for expert  $k$  at block  $l$ . In contrast to low-rank or bottleneck configurations such as LoRA [14], we do not enforce strong dimensionality reduction:

$$W_{k,l}^{(1)} \in \mathbb{R}^{d' \times d}, \quad W_{k,l}^{(2)} \in \mathbb{R}^{d \times d'}, \quad d' \approx d \text{ or } d' > d.$$

This design choice stabilizes fine-tuning across large domain gaps particularly between natural and medical imagery and prevents loss of feature capacity in domain-specific subspaces. We empirically trade off adapter width  $d'$  against the number of attached layers: either using a small number of large adapters ( $d' > d$ ) attached to later blocks, or lightweight adapters ( $d' < d$ ) attached to all layers.

Our generative backbone follows the state-of-the-art Flux diffusion transformer architecture [21, 25], composed of  $L = 57$  transformer blocks, including 19 dual-stream and 38 single-stream blocks. Each dual block jointly processes text features  $z_t$  and image features  $z_i$  via cross-attention:

$$z'_i = \text{MSA}(z_i) + \text{CA}(z_i, z_t), \quad z'_t = \text{MSA}(z_t),$$

followed by independent FeedForward projections:

$$z_i^{(l+1)} = F_i(z'_i), \quad z_t^{(l+1)} = F_t(z'_t).$$

Single-stream blocks omit text conditioning and rely solely on self-attention and linear projection of the image stream.

Because the dual blocks mediate multi-modal fusion, they serve as natural attachment points for our guided adapters. We thus instantiate  $A_{k,l}$  within the FeedForward submodules of later dual transformer blocks—where semantic alignment between modalities is strongest—or uniformly across all blocks to study the trade-off between expressiveness and efficiency. For ablation, we also mirror this configuration in the up- and down-projection layers of single-stream blocks, enabling a systematic analysis of adapter placement.

Our design constitutes a new class of *routing-free, prior-guided residual experts*. Equations 4–5 define a deterministic mapping from semantic partitions to expert adapters, eliminating gating uncertainty and reducing training variance. This preserves the interpretability of expert specialization while maintaining the computational simplicity of standard diffusion transformers.

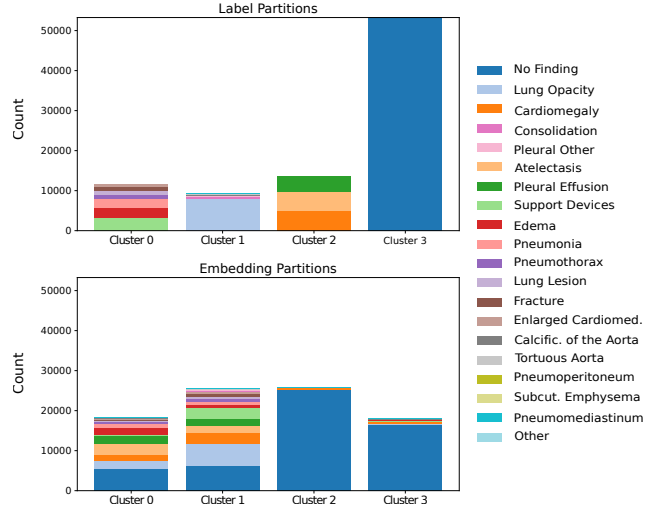


Figure 3. Composition of the partitioning based on labels (top) compared to the partitioning based on text clusters (bottom).

## 4. Experiments

**Datasets.** Motivated by our central goal of enabling more diverse and faithful image generation in medical imaging, we adopt MIMIC-CXR-LT [12] as our primary benchmark. This dataset extends the large-scale MIMIC-CXR collection [17] by introducing additional rare disease categories and constructing single-label splits to emphasize long-tail behavior. The resulting distribution poses a realistic challenge for generative modeling, capturing the severe frequency imbalance observed in real clinical data. We follow the official MIMIC-CXR-LT protocol, using 87,493 training samples to train our text-to-image diffusion model and 20,279 test-set prompts to generate synthetic images



Table 1. Class compositions of the MIMIC-CXR-LT [12] train and test splits.

Label	Train Count	Test Count
No Finding	53260	13987
Lung Opacity	7927	2108
Cardiomegaly	5113	1491
Atelectasis	4539	1117
Pleural Effusion	3832	1058
Support Devices	3279	964
Edema	2395	660
Pneumonia	2195	632
Pneumothorax	1172	323
Lung Lesion	1036	243
Fracture	791	239
Enlarged Cardiomediastinum	638	193
Consolidation	609	191
Pleural Other	254	69
Calcification of the Aorta	207	75
Tortuous Aorta	175	86
Pneumoperitoneum	32	35
Subcutaneous Emphysema	27	43
Pneumomediastinum	12	36

for evaluation. Both splits exhibit similar long-tailed characteristics, enabling consistent assessment of performance across head and tail classes. The detailed label statistics are summarized in Table 1.

Likewise, we base the evaluation of the classifier in our downstream task on NIH-CXR-LT [12]. This chest X-ray dataset is a split of ChestXray14 [35] with additional long-tail classes added. For evaluation, we take the proposed test split and filter any labels that are not part of MIMIC-CXR-LT, resulting in 16,506 samples.

To show the generalizability of our method, we conduct further experiments on the widely used Imagenet-LT [22] dataset. This allows us to verify our approach on a domain-unspecific long-tail setting. The train split consists of 115,846 image-label pairs, while the test split consists of 50,000 pairs.

**Metrics.** For the image generation, we want to reliably assess both the quality and diversity of the generated samples. To quantify the quality of the synthetic images, we utilize the common metrics Fréchet Inception Distance (FID) [10]. To assess the diversity of our generated samples, we employ Coverage [26], which is generally more robust to outliers than Improved Recall [18]. Given real features  $\Phi_r$  and generated features  $\Phi_g$ , the k-NearestNeighbours (kNN) radius around a sample  $x$  of  $\Phi$  is defined as

$$\rho_\Phi(x) := \|x - \text{NN}_k(x; \Phi \setminus \{x\})\|,$$

with the function indicating that  $x$  is within a kNN ball be-

ing defined as

$$f(x, \Phi) := \mathbf{1}[\exists y \in \Phi : \|x - y\| \leq \rho_\Phi(y)].$$

Based on this, Coverage estimates the fraction of real samples whose neighborhood contains at least one generated sample

$$\text{Cov} = \frac{1}{N} \sum_{i=1}^N \max_j \mathbf{1}[\|\varphi_r^{(i)} - \varphi_g^{(j)}\| \leq \rho_r(\varphi_r^{(i)})].$$

Since diversity is our primary concern, we report an additional robust diversity metric, called the adjusted Image Retrieval Score (IRS) [3]. For each image, this intuitive metric tries to retrieve the closest image in the training and test datasets, estimating which percentage of the datasets the synthetic images cover. The adjusted score is the test score normalized by the train score, which results in a metric that does not reward memorization, while keeping in mind the maximum possible coverage.

All image generation metrics are computed for a domain-specific DenseNet121 [15] as a feature extractor, which aligns with our downstream task and provides insights into radiographic properties of the generated images. For broader comparability, we also report features computed by the well-studied feature extractor DINOv2 [27], giving us insights into domain-unspecific features of our synthetic dataset. To gain robust estimates of our metrics, we generate 50,000 samples with resolution  $1024 \times 1024$  per model and training seed. For the evaluation of the classifier in the downstream task, we report the per-label results for the F1-score.

**Implementation Details & Computation Time.** The experiments were conducted using a checkpoint<sup>1</sup> of the state-of-the-art text-to-image foundation model Flux. Flux is a multimodal diffusion transformer trained via the flow-matching objective.

Since this base model was trained using CFG, we also performed our training and sampling with CFG enabled, using a moderate scale value of five. For each model, we fine-tuned the base Flux model for 10,000 steps, using an immediate batch size of eight. Each training run was conducted on eight NVIDIA H100 GPUs. Training a single model takes around 30 hours for full fine-tuning, and around 7-12 hours for the adapters, depending on the configuration.

For the MoCLE baseline, we used the same partitions and number of experts as in our own results. Using their best reported configuration, we kept the LoRA rank at 16.

Generating the synthetic training dataset for the classifier using a single diffusion model seed takes around 12 hours on eight NVIDIA H100 GPUs. Computing the features and metrics takes around 2 hours per model seed. The

<sup>1</sup><https://huggingface.co/black-forest-labs/FLUX.1-dev>

DenseNet-121 classifier in the downstream task was trained for 100 epochs using three seeds on each of the three seeded synthetic datasets, yielding nine runs per configuration.

**Image Metrics Results.** To evaluate chest X-ray image quality and diversity metrics, we consider features computed by a domain-specific feature encoder (Table 2), as well as domain-unspecific features (Table 3). Both tables show that using an adapter-based approach produces better results in terms of all metrics compared to full fine-tuning. However, while a learned gating function (MoCLE) or using a generic sequential adapter architecture (Label-all-512d(\*)) improves on the full fine-tuning baselines, they produce considerably weaker results than our GRASP adapters. In Table 2, the low-dimensional, all-layers adapter yields the most uniform gains and the best global FID. Meanwhile, relying on high-dim, last-layer adapters is slightly worse in the overall metrics, but can often outperform their counterparts on some labels, such as *Atelectasis*, *Edema*, or *Lung Opacity*. In the domain-unspecific results in Table 3, the high-dimensional, last-layers GRASP adapter clearly outperforms the other approaches. However, the low-dimensional, all-layers approach is still competitive in some labels.

On ImageNet-LT, DINOv2 results again favor the high-dimensional GRASP adapter, which achieves the strongest overall performance. Although MoCLE performs poorly on MIMIC-CXR-LT, it attains performance comparable to GRASP on ImageNet-LT, indicating it can be competitive on some datasets. We omit the macro average since the computations fail due to the small class sizes.

In summary, GRASP adapters outperform the baselines in most metrics, in particular in rare labels such as *Pneumoperitoneum*, which exhibit huge coverage and IRS peaks, indicating that our GRASP adapters considerably help in long-tail diversity. Using the all-labels approach seems to be slightly more faithful in terms of medical soundness, at the cost of a generally worse image generation.

**Downstream Classification Task.** Table 4 shows the classification performance of the Densenet-121 classifier in our single-label prediction task. The results are averaged across the three synthetic dataset seeds and the three classifier seeds, meaning each mean is calculated over nine runs. Due to the large imbalance in the data, the classification task is considerably difficult. This is evident in the results: the dominating class *No Finding* is the only class that can be predicted accurately, while most other classes have an F1-score of zero. This is in particular true for the full fine-tuning baselines, as well as the sequential adapter baseline, which manage to learn the dominating class very well, but have zero correct predictions for any other class. Meanwhile, the learned MoCLE adapters show a slightly broader range, gaining at least an average of 1.2% on *Edema*.

However, this fact is not only true for the synthetic

datasets: even when training on the real chest X-ray images, apart from *Pleural Effusion* and *Edema*, only the dominant class can be learned. This shows that the main issue lies in the difficulty of the classifier task and is not inherent to the synthetic data. Notably, this is the case despite the synthetic datasets being generated from the exact impressions of the real chest X-ray images. Therefore, they are supposed to cover roughly the same distribution.

The GRASP adapters have by far the highest versatility of the tested models, being able to obtain correct predictions for nine out of the thirteen classes. The classes the GRASP adapters did not manage to cover, all belong to the far end of the long-tail (see Table 1), with each of them only comprising of a couple of examples, making these especially hard to learn. However, the gains are small, and come at the cost of a lower head class performance.

Nonetheless, the GRASP adapters enable the classification model to achieve by far the highest overall F1-scores by label. They manage to produce roughly the same macro average as the real chest X-ray images, while being able to predict nine out of thirteen classes, instead of only three. Due to this reason, we see promise in the GRASP adapters in helping to create synthetic datasets that might help in such complex downstream tasks.

**Impact of Partitioning & Resampling.** To investigate whether our model can benefit from introducing resampling, we implement a simple resampling technique in which three items in the batch are resampled from the expert clusters in a round-robin manner, giving priority to experts with the least number of samples assigned to them. This way, we can guarantee that every expert has at least one sample per training step. We investigate the effect of resampling for both the label-wise and K-means partitions. As demonstrated in Table 5, using K-means clustering instead of our naive label-wise partitioning yields slightly lower results. However, the delta is very small, which would hint at the GRASP adapters exhibiting some robustness against the choice of sample partitioning. Table 5 further shows that resampling gives a small boost in overall diversity, without changing the overall quality. Additionally, resampling means that no unused parameters exist, which is suitable for optimizing gradient computation. Therefore, we recommend combining it with the adapters, despite us not using it in our main results to keep our adapters simple.

**Expert Utilization & Difference between Experts.** An important question is whether the observed performance gain truly arises from expert specialization, or whether it is primarily driven by another underlying mechanism. Figure 4 (a) shows the degree of specialization in terms of label-wise diversity of each expert. Expert 3, which was only trained on the *No Finding* label, shows worse performance in almost all labels, except its target label, compared to the other three mixed experts. This is an intuitive result,

Table 2. CXR Features: Per-label Coverage (Cov.)  $\uparrow$ , IRS  $\uparrow$ , and FID  $\downarrow$  across models. Baseline results are shown for full fine-tuning (Full-class and Full-text-class), training using a single expert consisting of adapters with a hidden dimension of 512 attached to all diffusion blocks (Label-all-512d(\*)), and MoCLE [9]. We report our results for low-dimensional adapter attached to all layers and high-dimensional adapters attached to the last few layers.

Label	Baselines												Ours											
	Full-class			Full-text-class			MoCLE [9]			Label-all(*)-512d			Label-all-512d			Label-all-16d			Label-4-4096d					
	Cov. $\uparrow$	IRS $\uparrow$	FID $\downarrow$	Cov. $\uparrow$	IRS $\uparrow$	FID $\downarrow$	Cov. $\uparrow$	IRS $\uparrow$	FID $\downarrow$	Cov. $\uparrow$	IRS $\uparrow$	FID $\downarrow$	Cov. $\uparrow$	IRS $\uparrow$	FID $\downarrow$	Cov. $\uparrow$	IRS $\uparrow$	FID $\downarrow$	Cov. $\uparrow$	IRS $\uparrow$	FID $\downarrow$	Cov. $\uparrow$	IRS $\uparrow$	FID $\downarrow$
Atelectasis	.56 $\pm$ .06	.09 $\pm$ .01	.19 $\pm$ .01	.61 $\pm$ .05	.1 $\pm$ .0	.18 $\pm$ .01	.85 $\pm$ .05	.23 $\pm$ .01	.12 $\pm$ .01	.88 $\pm$ .01	.26 $\pm$ .02	.09 $\pm$ .01	.93 $\pm$ .01	.44 $\pm$ .01	.05 $\pm$ .0	.93 $\pm$ .0	.55 $\pm$ .04	.04 $\pm$ .0	.95 $\pm$ .01	.56 $\pm$ .01	.03 $\pm$ .0	.95 $\pm$ .01	.56 $\pm$ .01	.03 $\pm$ .0
Cardiomegaly	.76 $\pm$ .04	.14 $\pm$ .01	.11 $\pm$ .01	.81 $\pm$ .03	.16 $\pm$ .01	.1 $\pm$ .01	.82 $\pm$ .01	.27 $\pm$ .01	.09 $\pm$ .01	.9 $\pm$ .01	.32 $\pm$ .01	.07 $\pm$ .01	.92 $\pm$ .01	.52 $\pm$ .03	.04 $\pm$ .0	.84 $\pm$ .0	.48 $\pm$ .01	.05 $\pm$ .0	.83 $\pm$ .01	.45 $\pm$ .03	.05 $\pm$ .0	.83 $\pm$ .01	.45 $\pm$ .03	.05 $\pm$ .0
Consolidation	.64 $\pm$ .02	.09 $\pm$ .0	.17 $\pm$ .01	.68 $\pm$ .03	.12 $\pm$ .01	.15 $\pm$ .01	.81 $\pm$ .04	.23 $\pm$ .0	.11 $\pm$ .0	.86 $\pm$ .05	.29 $\pm$ .03	.08 $\pm$ .01	.95 $\pm$ .01	.49 $\pm$ .04	.04 $\pm$ .01	.97 $\pm$ .0	.61 $\pm$ .07	.02 $\pm$ .0	.98 $\pm$ .0	.59 $\pm$ .06	.02 $\pm$ .0	.98 $\pm$ .0	.59 $\pm$ .06	.02 $\pm$ .0
Edema	.64 $\pm$ .07	.1 $\pm$ .01	.18 $\pm$ .01	.64 $\pm$ .03	.11 $\pm$ .01	.17 $\pm$ .02	.86 $\pm$ .03	.32 $\pm$ .02	.07 $\pm$ .01	.88 $\pm$ .02	.28 $\pm$ .02	.08 $\pm$ .0	.94 $\pm$ .02	.49 $\pm$ .04	.04 $\pm$ .01	.94 $\pm$ .05	.53 $\pm$ .03	.05 $\pm$ .0	.89 $\pm$ .01	.59 $\pm$ .05	.04 $\pm$ .01	.89 $\pm$ .01	.59 $\pm$ .05	.04 $\pm$ .01
Enlarged Cardiome.	.81 $\pm$ .04	.23 $\pm$ .02	.04 $\pm$ .01	.87 $\pm$ .03	.26 $\pm$ .01	.03 $\pm$ .0	.99 $\pm$ .0	.49 $\pm$ .0	.03 $\pm$ .0	.99 $\pm$ .01	.59 $\pm$ .01	.01 $\pm$ .0	.99 $\pm$ .01	.81 $\pm$ .07	.01 $\pm$ .0	.94 $\pm$ .05	.71 $\pm$ .09	.02 $\pm$ .0	.99 $\pm$ .01	.68 $\pm$ .06	.01 $\pm$ .0	.99 $\pm$ .01	.68 $\pm$ .06	.01 $\pm$ .0
Fracture	.7 $\pm$ .04	.15 $\pm$ .0	.04 $\pm$ .0	.71 $\pm$ .03	.17 $\pm$ .01	.04 $\pm$ .0	.93 $\pm$ .02	.42 $\pm$ .02	.02 $\pm$ .0	.92 $\pm$ .02	.37 $\pm$ .03	.02 $\pm$ .0	.1.0 $\pm$ .01	.51 $\pm$ .02	.01 $\pm$ .0	.99 $\pm$ .0	.51 $\pm$ .05	.01 $\pm$ .0	.99 $\pm$ .0	.47 $\pm$ .07	.01 $\pm$ .0	.99 $\pm$ .0	.47 $\pm$ .07	.01 $\pm$ .0
Lung Lesion	.48 $\pm$ .05	.12 $\pm$ .01	.07 $\pm$ .0	.65 $\pm$ .02	.14 $\pm$ .0	.06 $\pm$ .01	.83 $\pm$ .05	.29 $\pm$ .01	.04 $\pm$ .0	.81 $\pm$ .02	.33 $\pm$ .02	.03 $\pm$ .0	.95 $\pm$ .01	.54 $\pm$ .05	.01 $\pm$ .0	.1.0 $\pm$ .0	.55 $\pm$ .11	.0 $\pm$ .0	.99 $\pm$ .0	.54 $\pm$ .03	.01 $\pm$ .0	.99 $\pm$ .0	.54 $\pm$ .03	.01 $\pm$ .0
Lung Opacity	.51 $\pm$ .02	.09 $\pm$ .01	.13 $\pm$ .01	.59 $\pm$ .01	.11 $\pm$ .0	.12 $\pm$ .01	.82 $\pm$ .01	.26 $\pm$ .01	.06 $\pm$ .0	.85 $\pm$ .03	.3 $\pm$ .03	.04 $\pm$ .01	.95 $\pm$ .02	.5 $\pm$ .02	.01 $\pm$ .0	.99 $\pm$ .0	.59 $\pm$ .01	.01 $\pm$ .0	.99 $\pm$ .0	.57 $\pm$ .02	.01 $\pm$ .0	.99 $\pm$ .0	.57 $\pm$ .02	.01 $\pm$ .0
No Finding	.58 $\pm$ .0	.13 $\pm$ .0	.02 $\pm$ .0	.67 $\pm$ .0	.19 $\pm$ .01	.01 $\pm$ .0	.85 $\pm$ .01	.31 $\pm$ .01	.02 $\pm$ .0	.86 $\pm$ .01	.31 $\pm$ .01	.01 $\pm$ .0	.83 $\pm$ .01	.25 $\pm$ .01	.03 $\pm$ .0	.93 $\pm$ .0	.45 $\pm$ .01	.01 $\pm$ .0	.89 $\pm$ .01	.32 $\pm$ .01	.02 $\pm$ .0	.89 $\pm$ .01	.32 $\pm$ .01	.02 $\pm$ .0
Pleural Effusion	.38 $\pm$ .05	.07 $\pm$ .01	.45 $\pm$ .02	.46 $\pm$ .07	.08 $\pm$ .01	.41 $\pm$ .03	.59 $\pm$ .02	.21 $\pm$ .0	.29 $\pm$ .0	.58 $\pm$ .04	.21 $\pm$ .01	.28 $\pm$ .01	.65 $\pm$ .02	.27 $\pm$ .01	.22 $\pm$ .01	.65 $\pm$ .01	.34 $\pm$ .01	.2 $\pm$ .0	.62 $\pm$ .02	.31 $\pm$ .03	.2 $\pm$ .02	.62 $\pm$ .02	.31 $\pm$ .03	.2 $\pm$ .02
Pleural Other	.45 $\pm$ .04	.06 $\pm$ .0	.11 $\pm$ .0	.65 $\pm$ .03	.08 $\pm$ .01	.1 $\pm$ .01	.83 $\pm$ .03	.14 $\pm$ .02	.08 $\pm$ .0	.72 $\pm$ .01	.16 $\pm$ .02	.06 $\pm$ .0	.95 $\pm$ .03	.3 $\pm$ .05	.03 $\pm$ .01	.1.0 $\pm$ .0	.32 $\pm$ .08	.02 $\pm$ .0	.1.0 $\pm$ .0	.51 $\pm$ .13	.02 $\pm$ .0	.1.0 $\pm$ .0	.51 $\pm$ .13	.02 $\pm$ .0
Pneumonia	.55 $\pm$ .03	.13 $\pm$ .0	.1 $\pm$ .01	.64 $\pm$ .03	.17 $\pm$ .01	.09 $\pm$ .01	.77 $\pm$ .02	.26 $\pm$ .01	.07 $\pm$ .0	.76 $\pm$ .02	.32 $\pm$ .03	.05 $\pm$ .01	.92 $\pm$ .0	.55 $\pm$ .02	.02 $\pm$ .01	.95 $\pm$ .02	.61 $\pm$ .02	.01 $\pm$ .0	.95 $\pm$ .01	.53 $\pm$ .04	.01 $\pm$ .0	.95 $\pm$ .01	.53 $\pm$ .04	.01 $\pm$ .0
Pneumothorax	.39 $\pm$ .06	.08 $\pm$ .0	.26 $\pm$ .01	.53 $\pm$ .03	.1 $\pm$ .0	.23 $\pm$ .01	.59 $\pm$ .02	.17 $\pm$ .0	.18 $\pm$ .01	.64 $\pm$ .03	.18 $\pm$ .01	.15 $\pm$ .01	.78 $\pm$ .02	.33 $\pm$ .02	.1 $\pm$ .01	.89 $\pm$ .0	.41 $\pm$ .04	.07 $\pm$ .01	.83 $\pm$ .04	.37 $\pm$ .04	.08 $\pm$ .0	.83 $\pm$ .04	.37 $\pm$ .04	.08 $\pm$ .0
Support Devices	.61 $\pm$ .05	.11 $\pm$ .0	.09 $\pm$ .01	.75 $\pm$ .03	.15 $\pm$ .0	.08 $\pm$ .01	.97 $\pm$ .01	.91 $\pm$ .0	.03 $\pm$ .0	.98 $\pm$ .01	.44 $\pm$ .04	.02 $\pm$ .01	.99 $\pm$ .01	.63 $\pm$ .04	.01 $\pm$ .0	.98 $\pm$ .01	.58 $\pm$ .01	.01 $\pm$ .0	.99 $\pm$ .0	.59 $\pm$ .01	.01 $\pm$ .0	.99 $\pm$ .0	.59 $\pm$ .01	.01 $\pm$ .0
Pneumoperitoneum	.8 $\pm$ .1	.33 $\pm$ .05	.11 $\pm$ .01	.85 $\pm$ .12	.35 $\pm$ .05	.1 $\pm$ .02	.1.0 $\pm$ .0	.61 $\pm$ .06	.04 $\pm$ .01	.1.0 $\pm$ .0	.56 $\pm$ .0	.03 $\pm$ .0	.1.0 $\pm$ .0	.84 $\pm$ .07	.02 $\pm$ .0	.1.0 $\pm$ .0	.73 $\pm$ .14	.02 $\pm$ .0	.1.0 $\pm$ .0	.7 $\pm$ .05	.01 $\pm$ .0	.1.0 $\pm$ .0	.7 $\pm$ .05	.01 $\pm$ .0
Pneumomediastinum	.97 $\pm$ .0	.76 $\pm$ .08	.05 $\pm$ .0	.96 $\pm$ .04	.75 $\pm$ .07	.05 $\pm$ .01	.1.0 $\pm$ .0	.86 $\pm$ .04	.05 $\pm$ .01	.1.0 $\pm$ .0	.92 $\pm$ .0	.05 $\pm$ .0	.1.0 $\pm$ .0	.58 $\pm$ .07	.05 $\pm$ .01	.1.0 $\pm$ .0	.81 $\pm$ .07	.05 $\pm$ .05	.1.0 $\pm$ .0	.84 $\pm$ .0	.07 $\pm$ .01	.1.0 $\pm$ .0	.84 $\pm$ .0	.07 $\pm$ .01
Subcut. Emphysema	.41 $\pm$ .13	.19 $\pm$ .04	.37 $\pm$ .01	.57 $\pm$ .04	.28 $\pm$ .03	.35 $\pm$ .02	.7 $\pm$ .02	.43 $\pm$ .07	.25 $\pm$ .01	.71 $\pm$ .01	.49 $\pm$ .09	.2 $\pm$ .01	.79 $\pm$ .01	.55 $\pm$ .05	.17 $\pm$ .0	.91 $\pm$ .07	.57 $\pm$ .08	.11 $\pm$ .01	.84 $\pm$ .0	.51 $\pm$ .02	.13 $\pm$ .01	.84 $\pm$ .0	.51 $\pm$ .02	.13 $\pm$ .01
Tortuous Aorta	.81 $\pm$ .1	.18 $\pm$ .02	.05 $\pm$ .0	.92 $\pm$ .02	.27 $\pm$ .03	.03 $\pm$ .01	.99 $\pm$ .01	.43 $\pm$ .05	.03 $\pm$ .0	.95 $\pm$ .03	.51 $\pm$ .02	.02 $\pm$ .0	.1.0 $\pm$ .0	.81 $\pm$ .09	.0 $\pm$ .0	.95 $\pm$ .03	.8 $\pm$ .14	.01 $\pm$ .0	.97 $\pm$ .04	.63 $\pm$ .08	.01 $\pm$ .0	.97 $\pm$ .04	.63 $\pm$ .08	.01 $\pm$ .0
Calc. of the Aorta	.7 $\pm$ .07	.11 $\pm$ .01	.08 $\pm$ .0	.76 $\pm$ .06	.15 $\pm$ .01	.07 $\pm$ .0	.92 $\pm$ .03	.3 $\pm$ .04	.06 $\pm$ .0	.95 $\pm$ .02	.3 $\pm$ .03	.04 $\pm$ .0	.1.0 $\pm$ .01	.65 $\pm$ .15	.02 $\pm$ .0	.99 $\pm$ .02	.73 $\pm$ .09	.02 $\pm$ .0	.99 $\pm$ .02	.5 $\pm$ .06	.02 $\pm$ .0	.99 $\pm$ .02	.5 $\pm$ .06	.02 $\pm$ .0
All labels	.55 $\pm$ .01	.11 $\pm$ .0	.06 $\pm$ .01	.65 $\pm$ .01	.16 $\pm$ .01	.05 $\pm$ .01	.84 $\pm$ .01	.32 $\pm$ .01	.04 $\pm$ .0	.86 $\pm$ .01	.33 $\pm$ .02	.03 $\pm$ .0	.9 $\pm$ .01	.35 $\pm$ .01	.02 $\pm$ .0	.94 $\pm$ .0	.5 $\pm$ .0	.01 $\pm$ .0	.92 $\pm$ .01	.41 $\pm$ .01	.02 $\pm$ .0	.92 $\pm$ .01	.41 $\pm$ .01	.02 $\pm$ .0
Macro Avg	.62 $\pm$ .16	.17 $\pm$ .16	.14 $\pm$ .11	.7 $\pm$ .13	.2 $\pm$ .15	.12 $\pm$ .1	.85 $\pm$ .12	.35 $\pm$ .17	.09 $\pm$ .07	.85 $\pm$ .12	.37 $\pm$ .17	.07 $\pm$ .07	.92 $\pm$ .1	.53 $\pm$ .17	.05 $\pm$ .06	.92 $\pm$ .09	.56 $\pm$ .12	.04 $\pm$ .05	.91 $\pm$ .1	.52 $\pm$ .1	.04 $\pm$ .05	.91 $\pm$ .1	.52 $\pm$ .1	.04 $\pm$ .05

Table 3. DINOv2: Features: Per-label Coverage (Cov.)  $\uparrow$ , IRS  $\uparrow$ , and FID  $\downarrow$  across models. Baseline results are shown for full fine-tuning (Full-class and Full-text-class), training using a single expert consisting of adapters with a hidden dimension of 512 attached to all diffusion blocks (Label-all-512d(\*)), and MoCLE [9]. We report our results for low-dimensional adapter attached to all layers and high-dimensional adapters attached to the last few layers. Note that for Imagenet-LT, we only have one full fine-tuning baseline, since there are no captions.

	Method	MIMIC-CXR-LT						Imagenet-LT		
		All labels			Macro Avg			All labels		
		Cov. $\uparrow$	IRS $\uparrow$	FID $\downarrow$	Cov. $\uparrow$	IRS $\uparrow$	FID $\downarrow$	Cov. $\uparrow$	IRS $\uparrow$	FID $\downarrow$
Baseline	Full-class	.01 $\pm$ .0	.08 $\pm$ .01	106.6 $\pm$ 14.2	.07 $\pm$ .05	.22 $\pm$ .11	145.5 $\pm$ 28.5	.71 $\pm$ .01	.76 $\pm$ .01	155.1 $\pm$ 5.5
	Full-text-class	.02 $\pm$ .01	.12 $\pm$ .02	88.3 $\pm$ 12.6	.11 $\pm$ .07	.27 $\pm$ .14	128.3 $\pm$ 29.1	.71 $\pm$ .01	.76 $\pm$ .01	155.1 $\pm$ 5.5
	MoCLE [9]	.02 $\pm$ .0	.13 $\pm$ .0	87.5 $\pm$ .43	.15 $\pm$ .11	.29 $\pm$ .14	123.0 $\pm$ 29.2	.75 $\pm$ .0	.76 $\pm$ .0	109.4 $\pm$ .1
	Label-all-512d(*)	.02 $\pm$ .0	.15 $\pm$ .01	80.9 $\pm$ 4.2	.14 $\pm$ .1	.34 $\pm$ .17	119.9 $\pm$ 33.2	.57 $\pm$ .0	.39 $\pm$ .0	249.9 $\pm$ 10.4
Ours	Label-all-512d	.02 $\pm$ .0	.17 $\pm$ .0	76.6 $\pm$ .54	.17 $\pm$ .12	.37 $\pm$ .17	115.4 $\pm$ 39.2	.67 $\pm$ .07	.70 $\pm$ .22	164.4 $\pm$ 60.2
	Label-all-16d	.01 $\pm$ .0	.17 $\pm$ .0	91.4 $\pm$ .6	.12 $\pm$ .1	.38 $\pm$ .17	150.6 $\pm$ 76.2	.70 $\pm$ .0	.81 $\pm$ .0	132.3 $\pm$ 2.2
	Label-4-4096d	.03 $\pm$ .0	.19 $\pm$ .0	67.3 $\pm$ .6	.23 $\pm$ .16	.39 $\pm$ .18	107.7 $\pm$ 33.3	.75 $\pm$ .0	.80 $\pm$ .01	109.4 $\pm$ .1

since it implies that the pureness of the partition affects the specificity of an expert. There are also some other visible signs of a relationship between partition composition and expert performance. For example, Expert 0 performs the best for *Enlarged Mediastinum* and *Fracture*, and its cluster indeed has by far the largest share of these labels. In a similar vein, Expert 1 consists mostly of the *Lung Opacity* label, which results in this being the only label where the expert performs best, just to name a few examples. While a clear trend for this relationship between cluster composition and performance is visible, there also exist some outliers, such as Expert 3 performing better for *Edema* than Expert 0, despite their cluster compositions suggesting the contrary. We suspect the main reason for some noise being present is the specific composition of labels potentially being helpful for generalizability, or still causing gradient

conflicts. Additionally, the labels are not perfectly accurate in all cases, which might introduce some noise.

Table 6 shows expert utilization based on the type of cluster and whether resampling was used. Although the label-based cluster without resampling has a highly imbalanced utilization distribution compared to the experts based on K-means clusters, it still manages to outperform it. This implies that the quality of the clusters has a higher impact on performance than raw expert utilization. However, we can see a measurable impact of utilization on model performance when comparing resampling with non-resampling as shown in Figure 4 (b). As expected, Expert 3, which loses utilization share, becomes strictly worse performance-wise, while the other experts receive performance boosts. However, this does not mean we have a guaranteed improvement in the other experts for each label, since some labels such as

Table 4. This table shows for our DenseNet-121 classifier the per-label F1 (mean $\pm$ sd) across our generated chest X-ray datasets. The last four classes consist of almost no samples, which is why the classifier was unable to learn them, resulting in the last four rows being all zeros.

Label	Real	Baselines			Ours			
	Real	Full-class	Full-text-class	MoCLE	Label-all-512d(*)	Label-all-16d	Label-all-512d	Label-4-4096d
No Finding	.881 $\pm$ .002	<b>.882<math>\pm</math>.000</b>	<b>.882<math>\pm</math>.000</b>	.881 $\pm$ .001	<b>.882<math>\pm</math>.000</b>	.868 $\pm$ .004	.872 $\pm$ .005	.848 $\pm$ .019
Pleural Effusion	<b>.130<math>\pm</math>.111</b>	.000 $\pm$ .000	.000 $\pm$ .000	.004 $\pm$ .005	.000 $\pm$ .000	.052 $\pm$ .011	.023 $\pm$ .008	.082 $\pm$ .065
Edema	.011 $\pm$ .011	.000 $\pm$ .000	.000 $\pm$ .000	.012 $\pm$ .011	.000 $\pm$ .000	.032 $\pm$ .004	<b>.061<math>\pm</math>.028</b>	.044 $\pm$ .031
Atelectasis	.000 $\pm$ .000	.000 $\pm$ .000	.000 $\pm$ .000	.000 $\pm$ .000	.000 $\pm$ .000	.016 $\pm$ .011	.003 $\pm$ .007	<b>.022<math>\pm</math>.014</b>
Cardiomegaly	.000 $\pm$ .000	.000 $\pm$ .000	.000 $\pm$ .000	.000 $\pm$ .000	.000 $\pm$ .000	.003 $\pm$ .004	.012 $\pm$ .007	<b>.020<math>\pm</math>.007</b>
Consolidation	.000 $\pm$ .000	.000 $\pm$ .000	.000 $\pm$ .000	.000 $\pm$ .000	.000 $\pm$ .000	<b>.014<math>\pm</math>.014</b>	.002 $\pm$ .002	.012 $\pm$ .017
Pneumonia	.000 $\pm$ .000	.000 $\pm$ .000	.000 $\pm$ .000	.000 $\pm$ .000	.000 $\pm$ .000	<b>.007<math>\pm</math>.008</b>	.004 $\pm$ .008	.007 $\pm$ .011
Pneumothorax	.000 $\pm$ .000	.000 $\pm$ .000	.000 $\pm$ .000	.000 $\pm$ .001	.000 $\pm$ .000	.004 $\pm$ .005	.003 $\pm$ .002	<b>.007<math>\pm</math>.009</b>
Subcut. Emphysema	.000 $\pm$ .000	.000 $\pm$ .000	.000 $\pm$ .000	.000 $\pm$ .000	.000 $\pm$ .000	.004 $\pm$ .007	<b>.004<math>\pm</math>.007</b>	.000 $\pm$ .000
Calc. of the Aorta	.000 $\pm$ .000	.000 $\pm$ .000	.000 $\pm$ .000	.000 $\pm$ .000	.000 $\pm$ .000	.000 $\pm$ .000	.000 $\pm$ .000	.000 $\pm$ .000
Pneumomediastinum	.000 $\pm$ .000	.000 $\pm$ .000	.000 $\pm$ .000	.000 $\pm$ .000	.000 $\pm$ .000	.000 $\pm$ .000	.000 $\pm$ .000	.000 $\pm$ .000
Pneumoperitoneum	.000 $\pm$ .000	.000 $\pm$ .000	.000 $\pm$ .000	.000 $\pm$ .000	.000 $\pm$ .000	.000 $\pm$ .000	.000 $\pm$ .000	.000 $\pm$ .000
Tortuous Aorta	.000 $\pm$ .000	.000 $\pm$ .000	.000 $\pm$ .000	.000 $\pm$ .000	.000 $\pm$ .000	.000 $\pm$ .000	.000 $\pm$ .000	.000 $\pm$ .000
<b>Macro Avg</b>	.079 $\pm$ .244	.068 $\pm$ .245	.068 $\pm$ .245	.069 $\pm$ .244	.068 $\pm$ .245	.077 $\pm$ .238	.076 $\pm$ .240	<b>.080<math>\pm</math>.232</b>

Table 5. Ablation on resampling and clustering. Higher is better for Cov/IRS; lower is better for FID.

Label	Resample	Embed	Cov $\uparrow$	IRS $\uparrow$	FID $\downarrow$
✓	—	—	.91 $\pm$ .1	.52 $\pm$ .1	<b>.04<math>\pm</math>.05</b>
✓	✓	—	<b>.92<math>\pm</math>.09</b>	<b>.52<math>\pm</math>.12</b>	<b>.04<math>\pm</math>.05</b>
—	✓	✓	.91 $\pm$ .1	.52 $\pm$ .16	.05 $\pm$ .06

Table 6. Expert usage percentages by partitioning and sampling method for MIMIC-CXR-LT.

Label	Embed	Resample	Expert 0 (%)	Expert 1 (%)	Expert 2 (%)	Expert 3 (%)
✓	—	—	13.01	10.34	15.44	61.20
✓	—	✓	24.03	19.78	17.08	39.11
—	✓	—	21.82	28.79	29.29	20.10
—	✓	✓	25.64	26.46	25.81	22.09

*Tortuous Aorta* exhibit strictly worse results. Nonetheless, as established in Table 5 and Section 4, resampling still yields some minor overall improvements, giving it some use.

**Limitations.** Although the downstream gains remain modest because of the difficulty of the long-tail setting, our results highlight that targeted improvements in generative balance can already translate into measurable task benefits. The challenge itself is substantial, and the observed progress indicates that the method is moving the right parts of the system.

## 5. Conclusion

We have introduced GRASP, a lightweight yet effective method to address gradient conflicts in long-tail text-to-image diffusion training. By sample-wise partitioning into semantically coherent clusters and fine-tuning with guided residual adapters, GRASP mitigates intra-group gradient interference without relying on learned routing. Our experi-

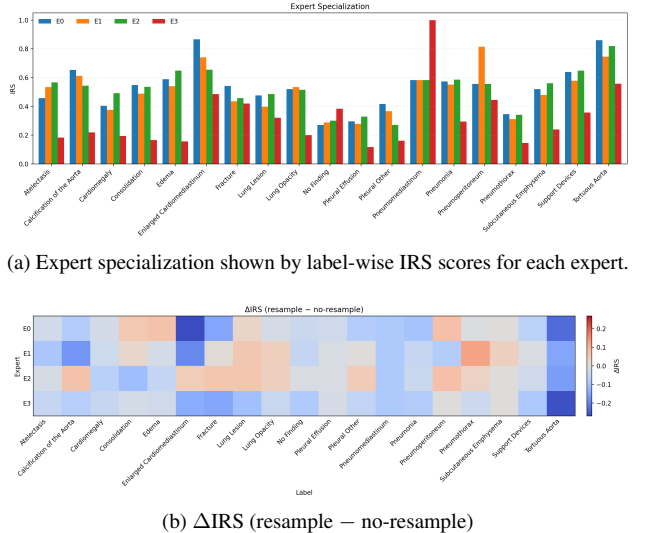


Figure 4. Comparison of expert specialization/resampling impact.

ments on MIMIC-CXR-LT, NIH-CXR-LT, and ImageNet-LT demonstrate that GRASP consistently improves both image quality and diversity, in particular for rare classes, while maintaining stability and scalability. The resulting synthetic data substantially enhances downstream classification for rare classes, narrowing the gap between real and generated distributions. Our results establish GRASP as a principled step toward distribution-aware fine-tuning of diffusion transformers. Future work will explore adaptive or hierarchical partitioning, universal experts for cross-cluster generalization, and the integration of GRASP with dynamic routing or reinforcement-based diversity objectives.



## References

- [1] Sumukh K Aithal, Pratyush Maini, Zachary Chase Lipton, and J Zico Kolter. Understanding hallucinations in diffusion models through mode interpolation. In *The Thirty-eighth Annual Conference on Neural Information Processing Systems*, 2024. 1
- [2] Prafulla Dhariwal and Alexander Nichol. Diffusion models beat gans on image synthesis. In *Advances in Neural Information Processing Systems*, pages 8780–8794. Curran Associates, Inc., 2021. 2
- [3] Mischa Dombrowski, Weitong Zhang, Sarah Cechnicka, Hadrien Reynaud, and Bernhard Kainz. Image generation diversity issues and how to tame them. In *Proceedings of the Computer Vision and Pattern Recognition Conference (CVPR)*, pages 3029–3039, 2025. 2, 5
- [4] Fang Dong, Mengyi Chen, Jixian Zhou, Yubin Shi, Yixuan Chen, Mingzhi Dong, Yujiang Wang, Dongsheng Li, Xiaochen Yang, Rui Zhu, Robert Dick, Qin Lv, Fan Yang, Tun Lu, Ning Gu, and Li Shang. Once read is enough: Domain-specific pretraining-free language models with cluster-guided sparse experts for long-tail domain knowledge. In *Advances in Neural Information Processing Systems*, pages 88956–88980. Curran Associates, Inc., 2024. 2, 4
- [5] Rafael Elberg, Denis Parra, and Mircea Petrache. Long Tail Image Generation Through Feature Space Augmentation and Iterated Learning. *arXiv preprint arXiv:2405.01705*, 2024. 2
- [6] Yixuan Feng and others. Routing Matters in MoE: Scaling Diffusion Transformers with Explicit Routing Guidance. *arXiv preprint arXiv:2510.24711*, 2025. 2
- [7] Emanuele Francazi, Marco Baity-Jesi, and Aurelien Lucchi. A theoretical analysis of the learning dynamics under class imbalance. In *Proceedings of the 40th International Conference on Machine Learning*, pages 10285–10322. PMLR, 2023. 2
- [8] Alireza Ganjdanesh, Yan Kang, Yuchen Liu, Richard Zhang, Zhe Lin, and Heng Huang. Mixture of Efficient Diffusion Experts Through Automatic Interval and Sub-Network Selection. In *European Conference on Computer Vision (ECCV)*, 2024. 2
- [9] Yunhao Gou, Zhili Liu, Kai Chen, Lanqing Hong, Hang Xu, Aoxue Li, Dit-Yan Yeung, James T Kwok, and Yu Zhang. Mixture of cluster-conditional lora experts for vision-language instruction tuning. *arXiv preprint arXiv:2312.12379*, 2023. 2, 7
- [10] Martin Heusel, Hubert Ramsauer, Thomas Unterthiner, Bernhard Nessler, and Sepp Hochreiter. Gans trained by a two time-scale update rule converge to a local nash equilibrium. In *Neural Information Processing Systems*, 2017. 5
- [11] Jonathan Ho and Tim Salimans. Classifier-free diffusion guidance. In *NeurIPS 2021 Workshop on Deep Generative Models and Downstream Applications*, 2021. 2
- [12] Gregory Holste, Song Wang, Ziyu Jiang, Thomas C. Shen, George Shih, Ronald M. Summers, Yifan Peng, and Zhangyang Wang. Long-tailed classification of thorax diseases on chest x-ray: A new benchmark study. In *Data Augmentation, Labelling, and Imperfections*, pages 22–32, Cham, 2022. Springer Nature Switzerland. 3, 4, 5
- [13] Yaxin Hou and Yuheng Jia. A square peg in a square hole: Meta-expert for long-tailed semi-supervised learning. In *Forty-second International Conference on Machine Learning*, 2025. 2, 3
- [14] Edward J Hu, yelong shen, Phillip Wallis, Zeyuan Allen-Zhu, Yuanzhi Li, Shean Wang, Lu Wang, and Weizhu Chen. LoRA: Low-rank adaptation of large language models. In *International Conference on Learning Representations*, 2022. 2, 4
- [15] Gao Huang, Zhuang Liu, Laurens van der Maaten, and Kilian Q Weinberger. Densely connected convolutional networks. In *Proceedings of the IEEE Conference on Computer Vision and Pattern Recognition*, 2017. 5
- [16] Shaohan Huang and Furu Wei. Mixture of lora experts. In *ICLR 2024*, 2024. 2
- [17] Alistair E. W. Johnson, Tom J. Pollard, Seth J. Berkowitz, Nathan R. Greenbaum, Matthew P. Lungren, Catherine Y. Deng, Roger G. Mark, and Steven Horng. Mimic-cxr, a de-identified publicly available database of chest radiographs with free-text reports. *Scientific Data*, 6(1):317, 2019. 4
- [18] Tuomas Kynkäänniemi, Tero Karras, Samuli Laine, Jaakko Lehtinen, and Timo Aila. Improved precision and recall metric for assessing generative models. *CoRR*, abs/1904.06991, 2019. 5
- [19] Yinghao Li, Vianne R. Gao, Chao Zhang, and MohamadAli Torkamani. Ensembles of low-rank expert adapters. In *The Thirtieth International Conference on Learning Representations*, 2025. 2
- [20] Yan Liang and others. Contrastive Conditional-Unconditional Alignment for Long-tailed Diffusion Model. *arXiv preprint arXiv:2507.09052*, 2025. 2
- [21] Yaron Lipman, Ricky TQ Chen, Heli Ben-Hamu, Maximilian Nickel, and Matt Le. Flow matching for generative modeling. *arXiv preprint arXiv:2210.02747*, 2022. 4
- [22] Ziwei Liu, Zhongqi Miao, Xiaohang Zhan, Jiayun Wang, Boqing Gong, and Stella X. Yu. Large-scale long-tailed recognition in an open world. In *IEEE Conference on Computer Vision and Pattern Recognition (CVPR)*, 2019. 5
- [23] Zichen Miao, Jiang Wang, Ze Wang, Zhengyuan Yang, Lijuan Wang, Qiang Qiu, and Zicheng Liu. Training diffusion models towards diverse image generation with reinforcement learning. In *Proceedings of the IEEE/CVF Conference on Computer Vision and Pattern Recognition (CVPR)*, pages 10844–10853, 2024. 2
- [24] Ana Montenegro and others. Causal Disentanglement for Robust Long-tail Medical Image Generation. *arXiv preprint arXiv:2504.14450*, 2025. 2
- [25] Mashrur M. Morshed and Vishnu Boddeti. Diverseflow: Sample-efficient diverse mode coverage in flows. In *Proceedings of the IEEE/CVF Conference on Computer Vision and Pattern Recognition (CVPR)*, pages 23303–23312, 2025. 1, 2, 4
- [26] Muhammad Ferjad Naeem, Seong Joon Oh, Youngjung Uh, Yunje Choi, and Jaejun Yoo. Reliable fidelity and diversity metrics for generative models. In *Proceedings of the*

- 37th International Conference on Machine Learning, pages 7176–7185. PMLR, 2020. [5](#)
- [27] Maxime Oquab, Timothée Darcet, Théo Moutakanni, Huy Vo, Marc Szafraniec, Vasil Khalidov, Pierre Fernandez, Daniel Haziza, Francisco Massa, Alaaeldin El-Nouby, Mahmoud Assran, Nicolas Ballas, Wojciech Galuba, Russell Howes, Po-Yao Huang, Shang-Wen Li, Ishan Misra, Michael Rabbat, Vasu Sharma, Gabriel Synnaeve, Hu Xu, Hervé Jegou, Julien Mairal, Patrick Labatut, Armand Joulin, and Piotr Bojanowski. Dinov2: Learning robust visual features without supervision, 2024. [5](#)
- [28] Daehee Park and 5 other authors. Generative Active Learning for Long-tail Trajectory Prediction via Controllable Diffusion Model. In *Proceedings of the IEEE/CVF International Conference on Computer Vision (ICCV)*, 2025. [2](#)
- [29] Sivaramakrishnan Rajaraman, Sha-E Yaacob, Subathra L. H, Sreejith S. G, and Sameer Antani. Addressing Class Imbalance with Latent Diffusion-based Data Augmentation for Improving Disease Classification in Pediatric Chest X-rays. *bioMethods*, 9(1), 2024. [2](#)
- [30] Robin Rombach, Andreas Blattmann, Dominik Lorenz, Patrick Esser, and Björn Ommer. High-resolution image synthesis with latent diffusion models. In *Proceedings of the IEEE/CVF Conference on Computer Vision and Pattern Recognition (CVPR)*, pages 10684–10695, 2022. [2](#)
- [31] Vikash Sehwal, Caner Hazirbas, Albert Gordo, Firat Ozgenel, and Cristian Canton Ferrer. Generating High Fidelity Data from Low-density Regions using Diffusion Models. In *2022 IEEE/CVF Conference on Computer Vision and Pattern Recognition (CVPR)*, pages 11482–11491, New Orleans, LA, USA, 2022. IEEE. [1](#), [2](#)
- [32] Noam Shazeer, \*Azalia Mirhoseini, \*Krzysztof Maziarz, Andy Davis, Quoc Le, Geoffrey Hinton, and Jeff Dean. Outrageously large neural networks: The sparsely-gated mixture-of-experts layer. In *International Conference on Learning Representations*, 2017. [2](#), [4](#)
- [33] Soobin Um and Jong Chul Ye. Self-Guided Generation of Minority Samples Using Diffusion Models. In *Computer Vision – ECCV 2024*, pages 414–430, Cham, 2025. Springer Nature Switzerland. [1](#), [2](#)
- [34] Soobin Um, Suhyeon Lee, and Jong Chul Ye. Don’t play favorites: Minority guidance for diffusion models. In *The Twelfth International Conference on Learning Representations*, 2024. [1](#), [2](#)
- [35] Xiaosong Wang, Yifan Peng, Le Lu, Zhiyong Lu, Mohammadhadi Bagheri, and Ronald M. Summers. ChestX-ray8: Hospital-scale chest x-ray database and benchmarks on weakly-supervised classification and localization of common thorax diseases. In *2017 IEEE Conference on Computer Vision and Pattern Recognition (CVPR)*. IEEE, 2017. [5](#)
- [36] Zeyue Xue, Guanglu Song, Qiushan Guo, Boxiao Liu, Zhuofan Zong, Yu Liu, and Ping Luo. RAPHAEL: Text-to-Image Generation via Large Mixture of Diffusion Paths. In *Advances in Neural Information Processing Systems (NeurIPS)*, pages 52187–52207, 2023. [2](#)
- [37] Hantao Zhang, Yuhe Liu, Jiancheng Yang, Shouhong Wan, Xinyuan Wang, Wei Peng, and Pascal Fua. LeFusion: Controllable Pathology Synthesis via Lesion-Focused Diffusion Models. In *International Conference on Learning Representations (ICLR)*, 2025. [2](#)
- [38] Tianjiao Zhang, Huangjie Zheng, Jiangchao Yao, Xiangfeng Wang, Mingyuan Zhou, Ya Zhang, and Yanfeng Wang. Long-tailed diffusion models with oriented calibration. In *The Twelfth International Conference on Learning Representations*, 2024. [2](#)
- [39] Zhe Zhao, Haibin Wen, Zikang Wang, Pengkun Wang, Fanfu Wang, Song Lai, Qingfu Zhang, and Yang Wang. Breaking long-tailed learning bottlenecks: A controllable paradigm with hypernetwork-generated diverse experts. In *Advances in Neural Information Processing Systems*, pages 7493–7520. Curran Associates, Inc., 2024. [2](#), [3](#)
- [40] Youwei Zheng, Yuxi Ren, Xin Xia, Xuefeng Xiao, and Xiaohua Xie. Dense2MoE: Restructuring Diffusion Transformer to MoE for Efficient Text-to-Image Generation. In *Proceedings of the IEEE/CVF International Conference on Computer Vision (ICCV)*, pages 18661–18670, 2025. [2](#)